

Full-Field Deformation Study of Ti–25Nb, Ti–25Nb–0.3O and Ti–25Nb–0.7O Shape Memory Alloys During Tension Using Digital Image Correlation



KAROL MAREK GOLASIŃSKI, MICHAŁ MAJ, WATARU TASAKI, ELŻBIETA ALICJA PIECZYSKA, and HEE YOUNG KIM

A Ti–25Nb shape memory alloy (SMA) exhibits shape memory effect associated with stress-induced martensitic transformation from β to α'' phase. Addition of oxygen stabilizes the β phase and changes stress–strain response. Oxygen-added Ti–25Nb SMAs show a more distinct superelastic behavior. In this work, digital image correlation (DIC) was applied to investigate for the first time full-field deformation of Ti–25Nb, Ti–25Nb–0.3O and Ti–25Nb–0.7O (at. pct) SMAs. The specimens were subjected to loading–unloading tensile tests to study local and global mechanical characteristics related to activity of particular deformation mechanisms of the SMAs. Strain and strain rate fields were quantitatively compared at selected stages of each SMA's deformation. It was found that the Ti–25Nb SMA exhibits a macroscopically localized Lüders-type deformation associated with the stress-induced phase transformation, whereas Ti–25Nb–0.3O and Ti–25Nb–0.7O SMAs show more discrete types of deformation related to activity of interstitial oxygen atoms. As a consequence, at particular stages of deformation, local values of strain rate of Ti–25Nb SMA were significantly higher than those of average strain rate. The results obtained in this paper provide a better understanding of the deformation mechanism in the oxygen-added Ti–25Nb based SMAs.

<https://doi.org/10.1007/s11661-024-07414-8>
© The Author(s) 2024

I. INTRODUCTION

IN the last three decades, a great focus has been placed on a development of biocompatible Ni-free β -Ti alloys for implant applications.^[1–8] It has been dictated by certain drawbacks of commonly used alloys, *i.e.*, high Young modulus of commercially pure titanium or Ti–6Al–4V alloy (greater than 100 GPa) when compared to that of the human bone (10–30 GPa), poor workability of Ti–Ni based shape memory alloys (SMAs) and Ni hypersensitivity.^[1,5,6] A relatively new group of Ti–Nb alloys can exhibit shape memory and superelastic

properties associated with martensitic transformation from body-centered cubic (β) to orthorhombic (α'') phase.^[8] However, oxygen-added Ti–Nb SMAs significantly change their mechanical behavior due to formation and activity of nanodomains, which hinder the long-range phase transformation.^[5,6,9,10] Consequently, the properties of the oxygen-added Ti–Nb SMAs include Young modulus lower than that of conventional Ti alloys, superelastic-like deformation and increased yield stress.

It is known that SMAs, specifically those based on Ti–Ni, exhibit inhomogeneous pseudoelastic deformation during tension, which is associated with a stress-induced martensitic transformation.^[11–17] A Lüders-type deformation of Ti–Ni was first observed in Ti–Ni wires subjected to tension.^[18,19] Several years later, experiments of thermomechanical aspects of Ti–Ni SMA were performed. It was shown that local measurements of strain and temperature serve to better understand the pseudoelastic behavior of the Ti–Ni SMA at different stages of loading and unloading. Initially, local deformation and temperature were monitored by miniature extensometers at up to four locations in the test section and by small thermocouples at up to six locations.^[11] Later, synchronized techniques of optical monitoring

KAROL MAREK GOLASIŃSKI is with the Multidisciplinary Research Center, Cardinal Stefan Wyszyński University in Warsaw, Dęwajtis 5, 01-815 Warsaw, Poland. Contact e-mail: k.golasinski@uksw.edu.pl MICHAŁ MAJ and ELŻBIETA ALICJA PIECZYSKA are with the Institute of Fundamental Technological Research, Polish Academy of Sciences, Pawińskiego 5b, 02-106 Warsaw, Poland. WATARU TASAKI and HEE YOUNG KIM are with the Division of Materials Science, Faculty of Pure and Applied Sciences, University of Tsukuba, Tsukuba, Ibaraki 305-8573, Japan. Manuscript submitted November 19, 2023; accepted April 17, 2024.

and infrared thermal imaging were applied to study the evolution of inhomogeneous deformation in SMA strips. The optical and thermal images were useful in clarifying the initiation and propagation of localized deformation of the Ti–Ni SMA during uniaxial experiments.^[12–14] After some years, a fast and sensitive infrared camera was applied to study nucleation and evolution of phase-transformation fronts in Reference 15 and development of transformation bands in the Ti–Ni SMA at various strain rates in Reference 16. Full-field quantitative strain fields were experimentally obtained for the first time by digital image correlation (DIC) in thin sheets of the Ti–Ni SMA.^[17] Since then, serious efforts have been done to get a better understanding about the deformation process of the Ti–Ni based and other SMAs. A review of applications of the full-field techniques used for thermomechanical characterization of various SMAs is given in Reference 20. Among others, DIC was employed to study local and global (average) strains and strain rates in SMAs.^[21] Tension, compression and compression-shear of Ti–Ni SMA was studied by means of DIC in the context of the stress-induced martensitic transformation in Reference 22 or strain-rate effects in Reference 23. Various deformation modes of superelastic Ti–Ni SMA tubes including tension, compression and bending were monitored by using DIC in Reference 24. To our best knowledge, full-field deformation of Ti–Nb based alloys has been seldom studied. Preliminary studies on local and average temperature changes of Gum Metal (Ti–23Nb–0.7Ta–2.0Zr–1.2O, at. pct) under tension were presented in Reference 25. More comprehensive thermomechanical investigation of Gum Metal subjected to tension at three strain rates was discussed in Reference 26. Energy storage and dissipation in consecutive tensile cycles of Gum Metal were macroscopically analyzed in Reference 27. In the case of Gum Metal, the martensitic transformation is suppressed by the addition of oxygen so that it is characterized by a nonlinear and superelastic-like deformation without hysteresis.^[28–33] No obvious activity of localized phase transformation was observed in temperature fields published in papers.^[25,26] However, a maximum drop of the average temperature of Gum Metal under tension corresponded to the strain value which was significantly lower than the recoverable strain. This finding is different when compared to the behavior of conventional alloys and proves an exothermic character of the superelastic-like deformation of Gum Metal under loading. Strain rate sensitivity,^[34] cyclic deformation^[35] and anisotropy^[36] of Gum Metal under tension were studied based on deformation fields obtained using DIC. Similar to the previously mentioned studies of Gum Metal under tension, the DIC results did not show special characteristics corresponding to a localized stress-induced phase transformation.

The objective of this work was to analyze and discuss global and local mechanical behavior of Ti–25Nb, Ti–25Nb–0.3O and Ti–25Nb–0.7O SMAs (at. pct) under load-unload tension. The compositions Ti–25Nb, Ti–25Nb–0.3O and Ti–25Nb–0.7O were selected to study the effect of the oxygen content on the gradual

suppression of the stress-induced martensitic transformation in the SMAs under tension using DIC. Constituent phase and microstructural features of as-fabricated SMAs were compared by means of scanning electron microscopy (SEM) and X-ray diffractometry (XRD). Subsequently, fields of Hencky strain and strain rate, determined by DIC, were analyzed at particular stages of deformation selected in stress–strain curves. The findings were compared to get a better understanding of the deformation of the oxygen-added Ti–25Nb based SMAs.

II. MATERIALS AND METHODS

The Ti–25Nb, Ti–25Nb–0.3O and Ti–25Nb–0.7O (at. pct) alloys were prepared by the Ar arc melting method using pre-melted sponges of Ti (Purity: > 99.7 pct) and pure Nb (Purity: 99.9 pct). The oxygen concentration of the alloys was adjusted by amount of TiO₂ powder (Purity: 99.9 pct). Homogeneity was ensured by repeated melting for six times and by flipping of the ingots between the melts. The ingots were sealed in a vacuumed quartz tube and homogenized at 1273 K for 120 minutes with subsequent air-cooling. Then the ingots were cold-rolled with a reduction in thickness of 95 pct. Specimens for XRD measurements, SEM and tensile tests were cut using an electro-discharge machine. The damaged surface was removed by mechanical polishing using SiC sandpapers and chemical etching using a solution with a composition of H₂O:HNO₃:HF = 5:4:1 (volume fraction). Specimens were solution-treated at 1173 K for 30 minutes in an Ar atmosphere, followed by water quenching. The oxidized surface was removed by chemical etching. SEM observations were made using a JEOL JSM-IT300 device. XRD measurements were conducted at room temperature with Cu K_α radiation using a Rigaku SmartLab apparatus. Displacement-controlled load-unload tensile tests of the SMAs were carried out using an MTS 858 testing machine at room temperature. Maximal displacement of 0.35 mm and displacement rate 0.06 mm s^{−1} were used. A technical drawing of the tested specimens is shown in Figure 1(a), whereas its photograph is presented in Figure 1(b). Taking into account the specimen's geometry, an average strain rate of 10^{−2} s^{−1} was applied. The gauge area of each specimen (4 mm × 6 mm) was covered with speckle patterns. The deformation process was monitored by a visible range sCMOS PCO Edge 5.5 camera. The image size was 931 pixels × 1280 pixels what gave pixel size equal to 7.7 μm. The recording frequency of the camera was 100 Hz. Mean Hencky strain $\bar{\epsilon}_{yy}$ was calculated on the basis of displacement fields obtained by DIC using so called 'virtual extensometers' of the initial length of 6 mm placed in the gage part of each specimen.

Hencky strain ϵ_{yy} and strain rate $\dot{\epsilon}_{yy}$ fields (where y is the loading direction) were determined on the basis of the displacement fields measured using 2D DIC method implemented in a ThermoCorr software. Examples of application of the ThermoCorr software for the DIC

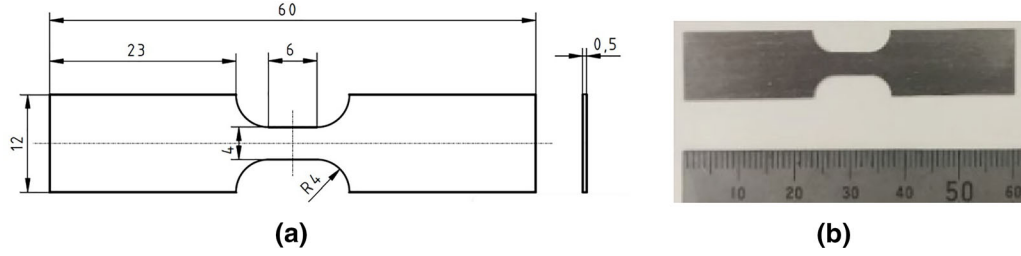


Fig. 1—(a) a technical drawing and (b) a photograph of the tested specimens.

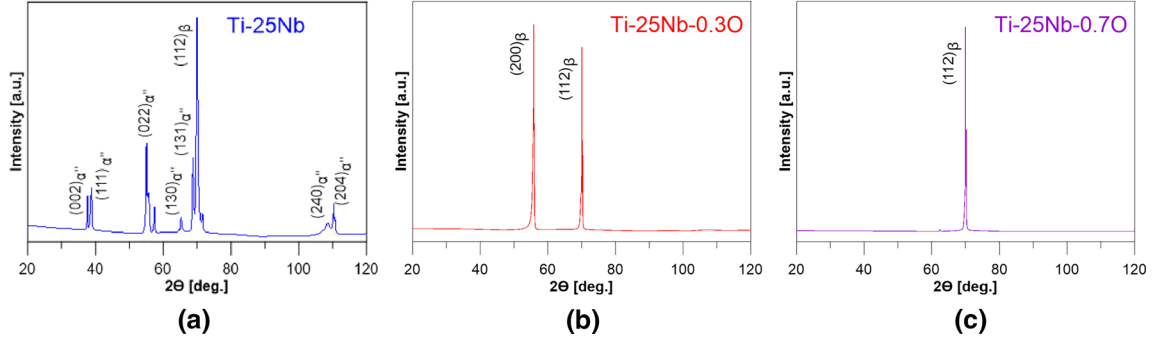


Fig. 2—XRD profiles of (a) Ti-25Nb, (b) Ti-25Nb-0.3O and (c) Ti-25Nb-0.7O SMAs.

analysis of Gum Metal, aluminum multicrystal and stainless steel are described in References 26, 34–40. The detailed numerical procedures are presented in Reference 37.

III. RESULTS AND DISCUSSION

A. Analysis of Constituent Phase and Microstructural Features of As-Fabricated SMAs

XRD profiles of the Ti-25Nb, Ti-25Nb-0.3O and Ti-25Nb-0.7O SMAs are presented in Figures 2(a) through (c), respectively. The α'' martensite phase and the β parent phase were observed in the Ti-25Nb alloy, whereas only the β parent phase was observed in the Ti-25Nb-0.3O and Ti-25Nb-0.7O alloys, indicating that the addition of oxygen stabilizes the β phase in these alloys.

Backscattered electron images taken by SEM of Ti-25Nb, Ti-25Nb-0.3O and Ti-25Nb-0.7O SMAs are presented in Figures 3(a) through (f). The microstructure of the Ti-25Nb SMA reveals needle-shaped α'' martensites in the β phase grains, as shown in Figures 3(a, b). Selected zones with α'' martensites were circled in Figure 3(b). In contrast, the microstructures of the oxygen-added Ti-25Nb-0.3O and Ti-25Nb-0.7O SMAs depict single β phase grains, as shown in Figures 3(c, d) and (e, f), respectively.

The microstructural observations of the SMAs are in line with the XRD results. They confirm that the addition of oxygen stabilizes the β phase in these alloys.

B. Mechanical Behavior of the SMAs Under Load–Unload Tension

Force–crosshead displacement and true stress–mean Hencky strain curves of Ti-25Nb, Ti-25Nb-0.3O and Ti-25Nb-0.7O SMAs under load–unload tension are compared in Figures 4(a) and (b), respectively.

In this study, characteristic parameters of the SMAs such as elastic modulus E , apparent yield stress σ_{YS} , superelastic strain $\bar{\epsilon}_{se}$, elastic strain $\bar{\epsilon}_e$, recovery strain $\bar{\epsilon}_r$ and plastic strain $\bar{\epsilon}_p$ were determined from stress–strain curves as schematically shown in Figure 5. For the sake of clarity, apparent yield stress σ_{YS} is the maximal stress values at which the stress–strain curve is still linear.

The Ti-25Nb SMA is known to exhibit shape memory effect.^[8] During loading, the Ti-25Nb alloy first deforms linearly and elastically with Young modulus $E = 88\text{GPa}$. When apparent yield stress $\sigma_{YS} = 150\text{MPa}$ is reached, the SMA starts deforming pseudoelastically. This phenomenon is associated with the martensitic transformation from β to α'' phase. It can be noticed that, after unloading, the superelastic strain was $\bar{\epsilon}_{se} = 0.95$ pct, the elastic strain was $\bar{\epsilon}_e = 0.29$ pct and the recovery strain was $\bar{\epsilon}_r = 1.24$ pct. In the case of Ti-25Nb alloy, the remaining strain $\bar{\epsilon}_p = 1.85$ pct can be recovered by heating, however, in this work the shape memory recovery was not studied.

In oxygen-added alloys, the β to α'' martensitic transformation is suppressed by generation of nanodomains. Oxygen atoms expand the surrounding Ti and Nb atoms, then generate and promote the shuffling and shearing mechanisms of the β to α'' martensitic

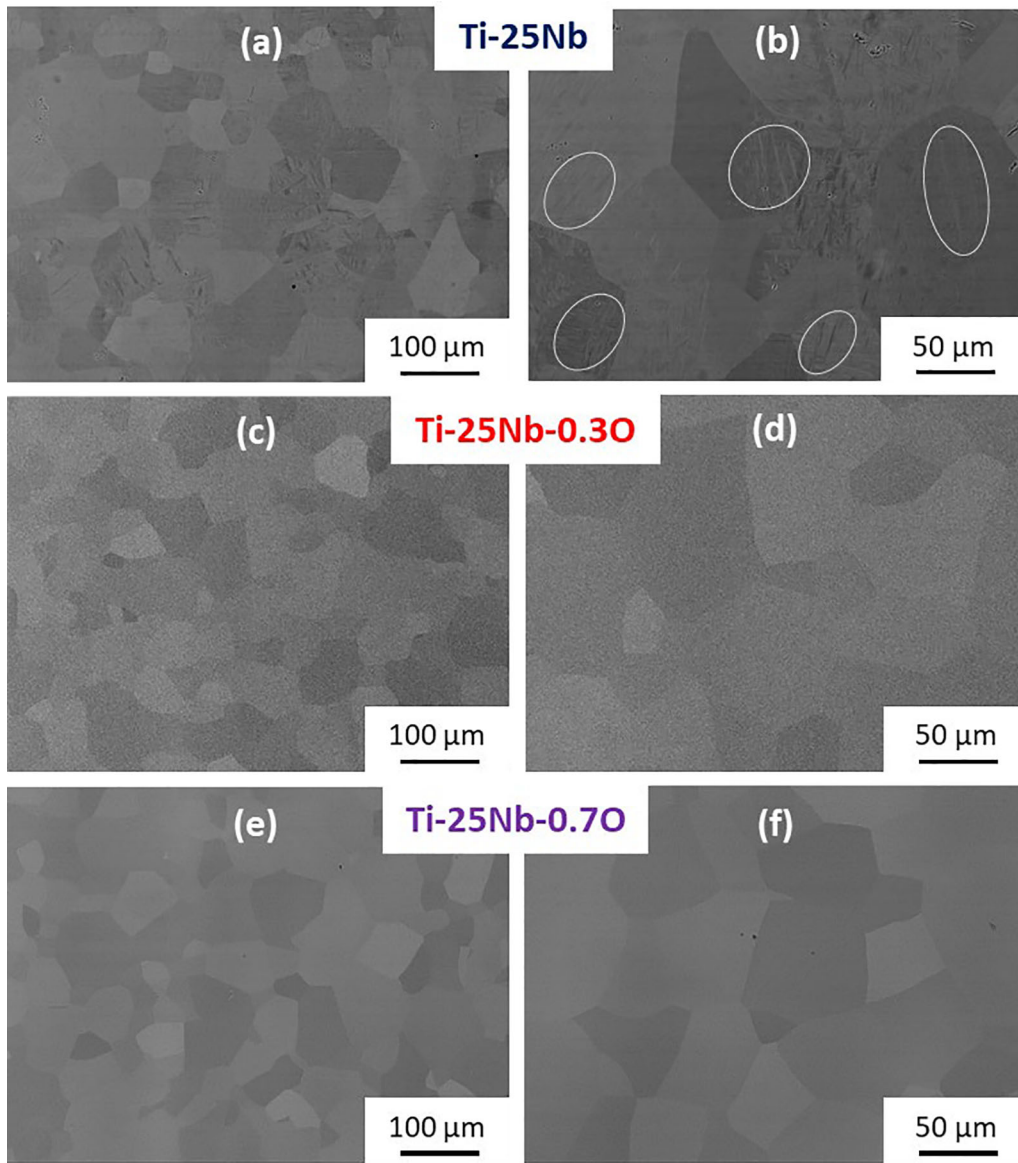


Fig. 3—Backscattered electron images of (a, b) Ti-25Nb, (c, d) Ti-25Nb-0.30 and (e, f) Ti-25Nb-0.70 SMAs.

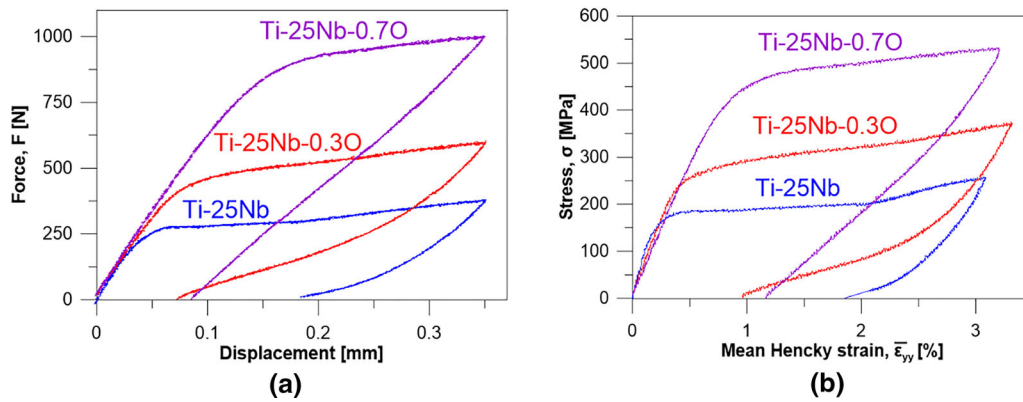


Fig. 4—Comparison of (a) force-displacement curves and (b) corresponding true stress-strain curves of Ti-25Nb, Ti-25Nb-0.30 and Ti-25Nb-0.70 SMAs under load-unload tension.

transformation.^[9,10] It causes the nonlinear superelastic-like deformation and the increase of flow stress. Similar phenomena were observed in the mechanical behavior of Gum Metal (Ti–23Nb–0.7Ta–2.0Zr–1.2O, at. pct).^[5,6,31,32] As a consequence, the Ti–25Nb–0.3O SMA was characterized by a Young’s modulus $E = 62$ GPa, apparent yield stress $\sigma_{YS} = 220$ MPa, total recovered strain $\bar{\epsilon}_r = 2.35$ pct, superelastic strain $\bar{\epsilon}_{se} = 1.79$ pct, elastic strain $\bar{\epsilon}_e = 0.56$ pct and remaining strain $\bar{\epsilon}_p = 0.96$ pct.

The Ti–25Nb–0.7O SMA was characterized by Young’s modulus of $E = 56$ GPa, apparent yield stress $\sigma_{YS} = 370$ MPa, total recovered strain of $\bar{\epsilon}_r = 2.05$ pct, superelastic strain $\bar{\epsilon}_{se} = 1.14$ pct, elastic strain $\bar{\epsilon}_e = 0.91$ pct and remaining strain $\bar{\epsilon}_p = 1.16$ pct.

The values of Young’s moduli E , apparent yield stresses σ_{YS} and four types of strains $\bar{\epsilon}_{se}$, $\bar{\epsilon}_e$, $\bar{\epsilon}_r$ and $\bar{\epsilon}_p$ of Ti–25Nb, Ti–25Nb–0.3O and Ti–25Nb–0.7O SMAs derived from stress–strain curves presented in Figure 4(b) are compared in Table I.

Young’s modulus tends to decrease with an increase in oxygen content. On the other hand, the apparent yield stress tends to increase with an increase in oxygen content. In the case of the Ti–25Nb SMA the total recovered strain was 1.24 pct. This alloy can exhibit

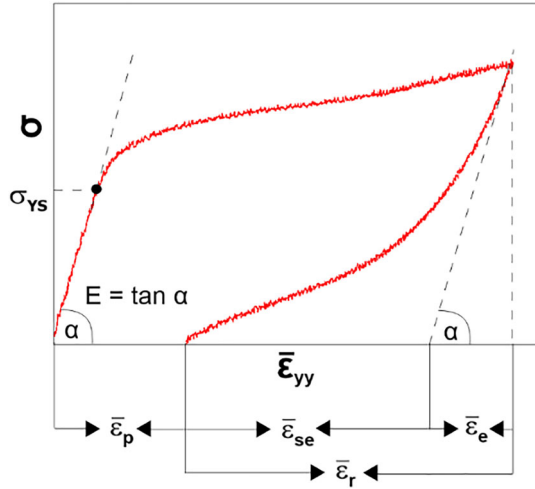


Fig. 5—A scheme of determination of parameters of elastic modulus E , apparent yield stress σ_{YS} , superelastic strain $\bar{\epsilon}_{se}$, elastic strain $\bar{\epsilon}_e$, recovery strain $\bar{\epsilon}_r$ and plastic strain $\bar{\epsilon}_p$ of the SMA from a stress–strain curve.

shape memory recovery when exposed to heat. In the case of oxygen-added SMAs, the total recovered strains were greater than 2 pct.

C. Full-Field Analysis of Mechanical Behavior of SMAs Under Load-Unload Tension

Seven critical stages of the SMAs deformation were selected based on the analysis of the stress–strain curves. The stages correspond to the following values of $\bar{\epsilon}_{yy}$.

$$\bar{\epsilon}_{yy} = 0.3 \text{ pct (during loading)} \quad [1]$$

$$\bar{\epsilon}_{yy} = 0.5 \text{ pct (during loading)} \quad [2]$$

$$\bar{\epsilon}_{yy} = 1.0 \text{ pct (during loading)} \quad [3]$$

$$\bar{\epsilon}_{yy} = 2.0 \text{ pct (during loading)} \quad [4]$$

$$\bar{\epsilon}_{yy} = \bar{\epsilon}_{\max} \text{ (maximal strain during loading)} \quad [5]$$

$$\bar{\epsilon}_{yy} = 2.5 \text{ pct (during unloading)} \quad [6]$$

$$\bar{\epsilon}_{yy} = \bar{\epsilon}_p \text{ (strain remaining after unloading)} \quad [7]$$

Evolution of ϵ_{yy} fields, where y is the direction of loading, at all selected stages are presented in Figure 6. The stages [1] through [7] are marked in the stress–strain curve and in ϵ_{yy} maps, correspondingly. To note, in this work the values set in scale bars for analysis of deformation fields are different and adjusted to particular stages of deformation.

The deformation of the Ti–25Nb SMA proceeds in an inhomogeneous manner from the very beginning (stage [1]), which approximately corresponds to the apparent yield stress. The ϵ_{yy} field determined at stage [1] clearly indicates a macroscopic onset of the stress-induced martensitic transformation from β to α'' phase, as seen through the needle-like microstructural features in Figure 3(b), which nucleates as a localized band on the top of the gauge part of the specimen. At stage [2], the second band starts nucleating in the other part of the specimen and the upper band develops. During loading [3]–[4], the two bands propagate towards the center of the specimen’s gage part. At the end of loading (stage [5]) the ϵ_{yy} field looks more homogenous and the bands

Table I. Measured Values of Elastic Moduli E , Apparent Yield Stresses σ_{YS} , Superelastic Strain $\bar{\epsilon}_{se}$, Elastic Strain $\bar{\epsilon}_e$, Recovery Strain $\bar{\epsilon}_r$ and Plastic Strain $\bar{\epsilon}_p$ of Ti–25Nb, Ti–25Nb–0.3O and Ti–25Nb–0.7O SMAs

Composition (At. Pct)	Young’s Modulus (GPa)	Apparent Yield Stress (MPa)	Strain (Pct)			
	E	σ_{YS}	$\bar{\epsilon}_r$	$\bar{\epsilon}_e$	$\bar{\epsilon}_{se}$	$\bar{\epsilon}_p$
Ti–25Nb	88	150	1.24	0.29	0.95	1.85
Ti–25Nb–0.3O	62	220	2.35	0.56	1.79	0.96
Ti–25Nb–0.7O	56	370	2.05	0.91	1.14	1.16

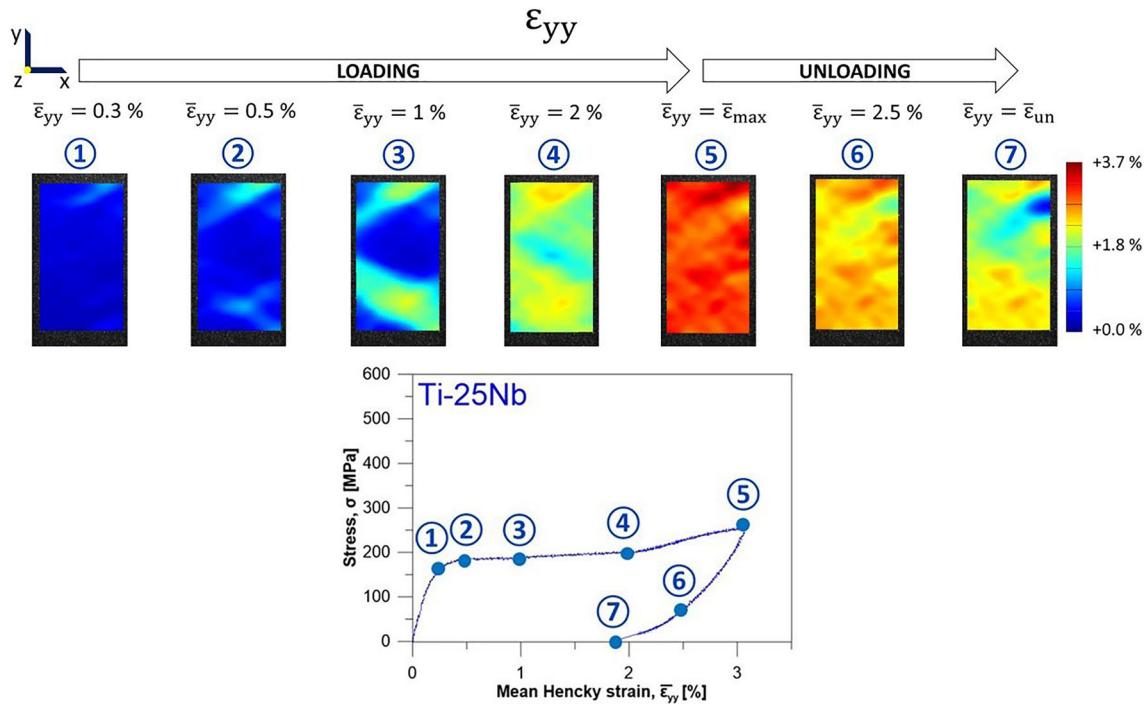


Fig. 6—Hencky strain ϵ_{yy} fields of a Ti-25Nb SMA under load-unload tension at selected stages of deformation.

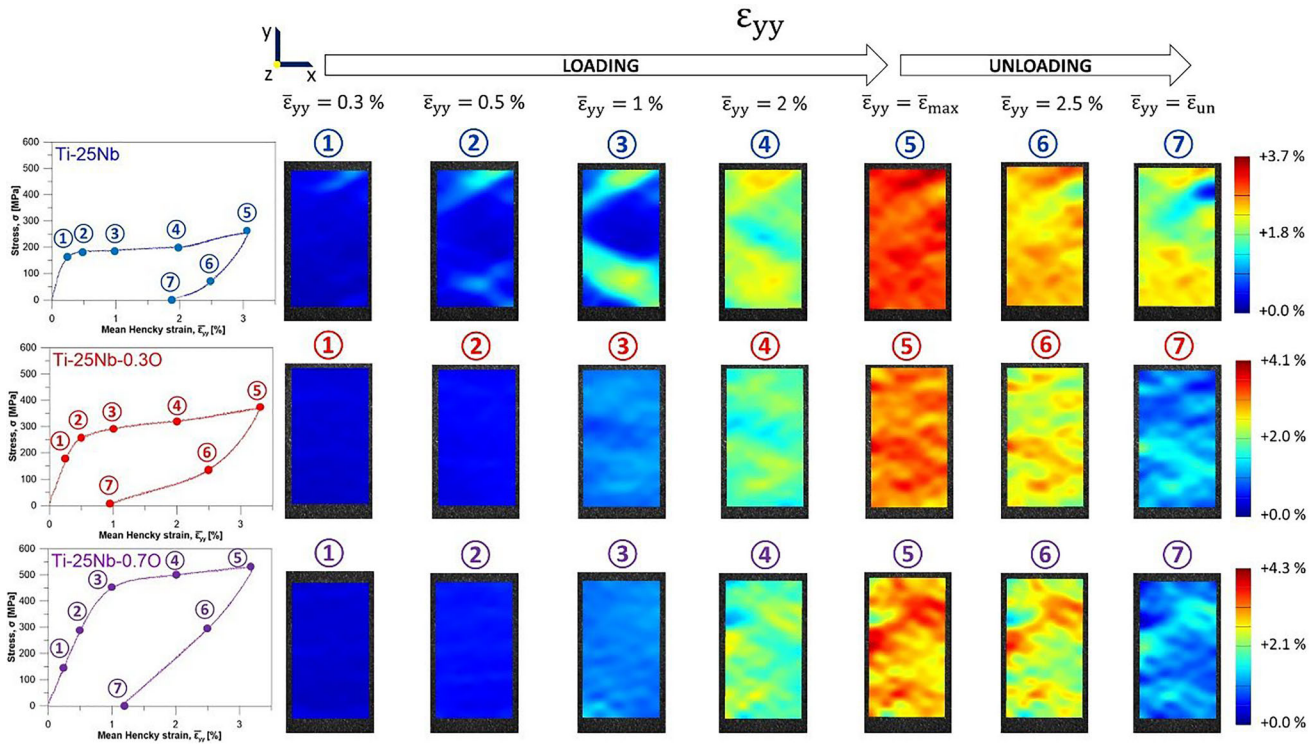


Fig. 7—Hencky strain ϵ_{yy} fields of Ti-25Nb, Ti-25Nb-0.30 and Ti-25Nb-0.70 SMAs under load-unload tension at selected stages of deformation with unified scales for each alloy.

cannot be clearly distinguished. During unloading [6]–[7], local strain values decrease significantly ($\Delta\epsilon_{yy} = 0.02$) in a small zone between the previously

developed bands of martensite, whereas in the major area of the specimen, the drop is moderate around $\Delta\epsilon_{yy} = 0.009$. The results are quite different when

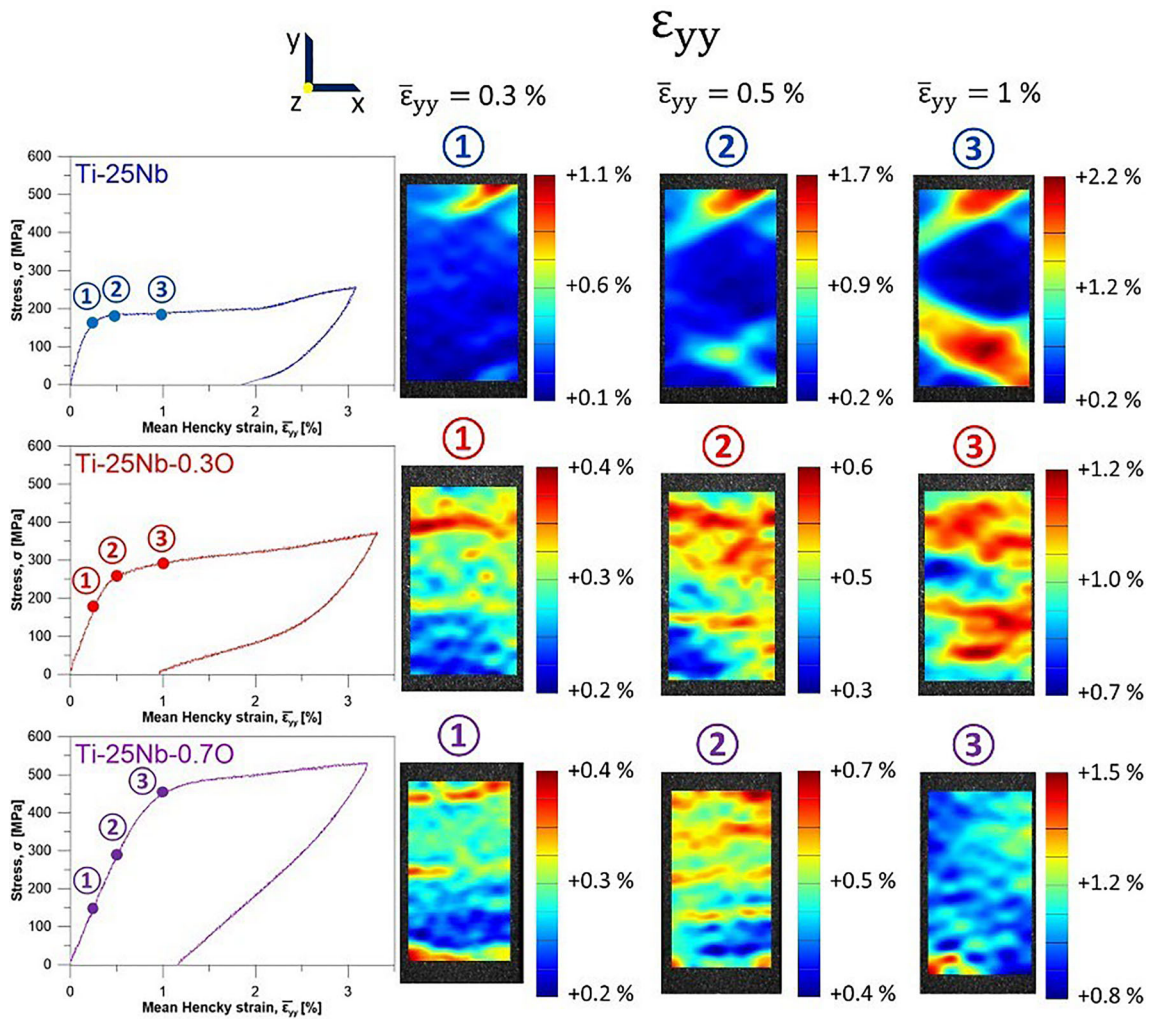


Fig. 8—Hencky strain ϵ_{yy} fields of Ti-25Nb, Ti-25Nb-0.3O and Ti-25Nb-0.7O SMAs under load-unload tension at selected stages of the initial deformation up to strain $\bar{\epsilon}_{yy} = 0.01$ with automatic scalebars.

compared to those obtained for the Ti-Ni SMA under load-unload tension. In the case of the Ti-Ni SMA, several relatively narrow bands generated by stress-induced martensitic transformation were captured using DIC.^[16]

A comparison of the Hencky strain ϵ_{yy} fields determined at selected stages [1] through [7] of the Ti-25Nb, Ti-25Nb-0.3O and Ti-25Nb-0.7O SMAs under load-unload tension is presented in Figure 7. The ϵ_{yy} fields indicate that the deformation processes of the oxygen-added SMAs are different and more discrete when compared to the one of the Ti-25Nb SMA. No dominant localized band of martensite can be observed in the case of the Ti-25Nb-0.3O and Ti-25Nb-0.7O SMAs.

For a detailed analysis of the initial deformation range, Hencky strain ϵ_{yy} fields of Ti-25Nb, Ti-25Nb-0.3O and Ti-25Nb-0.7O SMAs under tensile loading at stages corresponding to strains: $\bar{\epsilon}_{yy} = 0.3$ pct, $\bar{\epsilon}_{yy} = 0.5$ pct and $\bar{\epsilon}_{yy} = 1$ pct with automatically adjusted scalebars are presented in Figure 8. The

Ti-25Nb-0.3O SMA starts deforming in the upper part of the gauge section (stage [1]). At stage [2] corresponding approximately to the apparent yield stress, the ϵ_{yy} field develops also in the central part of the specimen.

During loading stages [3]–[4], the ϵ_{yy} fields concentrate in two zones located in the upper and lower parts of the gauge section. However, at stage [5], when $\bar{\epsilon}_{max}$ is reached, the ϵ_{yy} field looks more discrete, and the two zones cannot be clearly distinguished any longer. During unloading [5]–[6]–[7], the strain values decrease significantly in the upper part of the gauge section. Hence, when unloaded [7], the remaining strain is distributed mainly in the lower part of the gauge section.

The Ti-25Nb-0.7O SMA initially deforms in a relatively homogenous manner [1]–[2]. At stage [3] corresponding approximately to the apparent yield stress, the ϵ_{yy} field indicates slight concentrations in the left lower and right upper corners. During loading [4]–[5], three zones with significant values of strain develop. The unloading process ([5]–[6]–[7]) proceeds quite homogeneously. Local strain values decrease

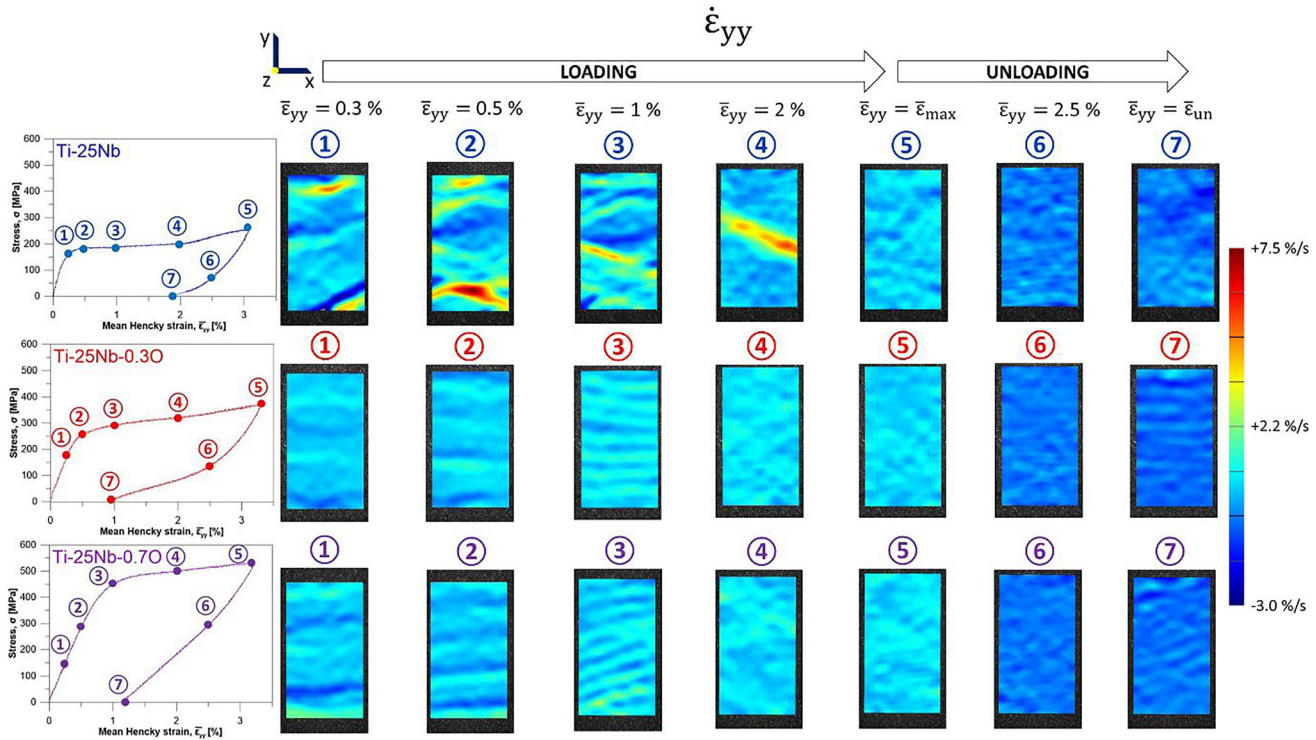


Fig. 9—Strain rate $\dot{\epsilon}_{yy}$ fields of Ti-25Nb, Ti-25Nb-0.30 and Ti-25Nb-0.70 SMAs under load-unload tension at selected stages of deformation with a unified scalebar.

significantly ($\Delta\epsilon_{yy} = 0.02$) in all parts of the gage section, but the distribution of the ϵ_{yy} field remains almost unchanged.

Strain rate $\dot{\epsilon}_{yy}$ fields of the Ti-25Nb, Ti-25Nb-0.30 and Ti-25Nb-0.70 SMAs under load-unload tension at selected stages of deformation are shown in Figure 9. In the case of the Ti-25Nb SMA, during the loading stages [1] through [4] the propagation fronts of the active phase transformation are clearly marked by high values of the local strain rate in the strain rate $\dot{\epsilon}_{yy}$ fields. At stage [2], local values of strain rate were over seven times higher (7.5 pct/s) than those of average strain rate. During the unloading stages [5]–[6]–[7], the local strain rate fronts are not too well pronounced. In the case of oxygen-added SMAs, there are no dominant bands. However, some more discrete but still rather localized features resulting from the superelastic deformation can be observed.

Maximal local values of strain rate were around two times higher than those of average strain rate at particular stages of deformation. In the case of the Ti-25Nb-0.30 SMA, maximal local value of $\dot{\epsilon}_{yy}$ was 1.7 pct/s at stage [5], whereas in the case of the Ti-25Nb-0.70 SMA, maximal local value of $\dot{\epsilon}_{yy}$ was 2.6 pct/s at stage [3].

Spatiotemporal graphs of Hencky strain ϵ_{yy} and strain rate $\dot{\epsilon}_{yy}$ of the Ti-25Nb, Ti-25Nb-0.30 and Ti-25Nb-0.70 SMAs under load-unload tension are shown in Figure 10. They present how a longitudinal profile located in the center of the gauge part of the specimen is changing in time.

The ϵ_{yy} graphs confirm that the Ti-25Nb SMA deformed in a localized manner starting in the upper part of the specimen's gage section and continuing in the lower part. Consequently, the $\dot{\epsilon}_{yy}$ graphs of the Ti-25Nb SMA show that local values of $\dot{\epsilon}_{yy}$ were significantly higher in the areas where the martensitic transformation was actively propagating when compared to the average $\dot{\epsilon}_{yy}$.

On the other hand, the ϵ_{yy} graphs of the oxygen-added SMAs prove that they do not exhibit Lüders-type deformation. The Ti-25Nb-0.30 and Ti-25Nb-0.70 SMAs have more discrete evolutions of ϵ_{yy} fields related to the activity of interstitial oxygen atoms. Similarly, the $\dot{\epsilon}_{yy}$ graphs of the Ti-25Nb-0.30 and Ti-25Nb-0.70 SMAs do not reveal areas of particularly high values of local strain rates $\dot{\epsilon}_{yy}$.

IV. CONCLUSIONS

Digital image correlation was used to investigate for the first time full-field deformation of Ti-25Nb, Ti-25Nb-0.30 and Ti-25Nb-0.70 (at. pct) SMAs under load-unload tension. Our investigation showed that local and global mechanical characteristics related to the activity of particular deformation mechanisms of the SMAs considered are quite different:

- (1) The Ti-25Nb SMA under tensile loading exhibited a macroscopically localized Lüders-type deformation in a form of two wide macroscopic bands associated with the stress-induced

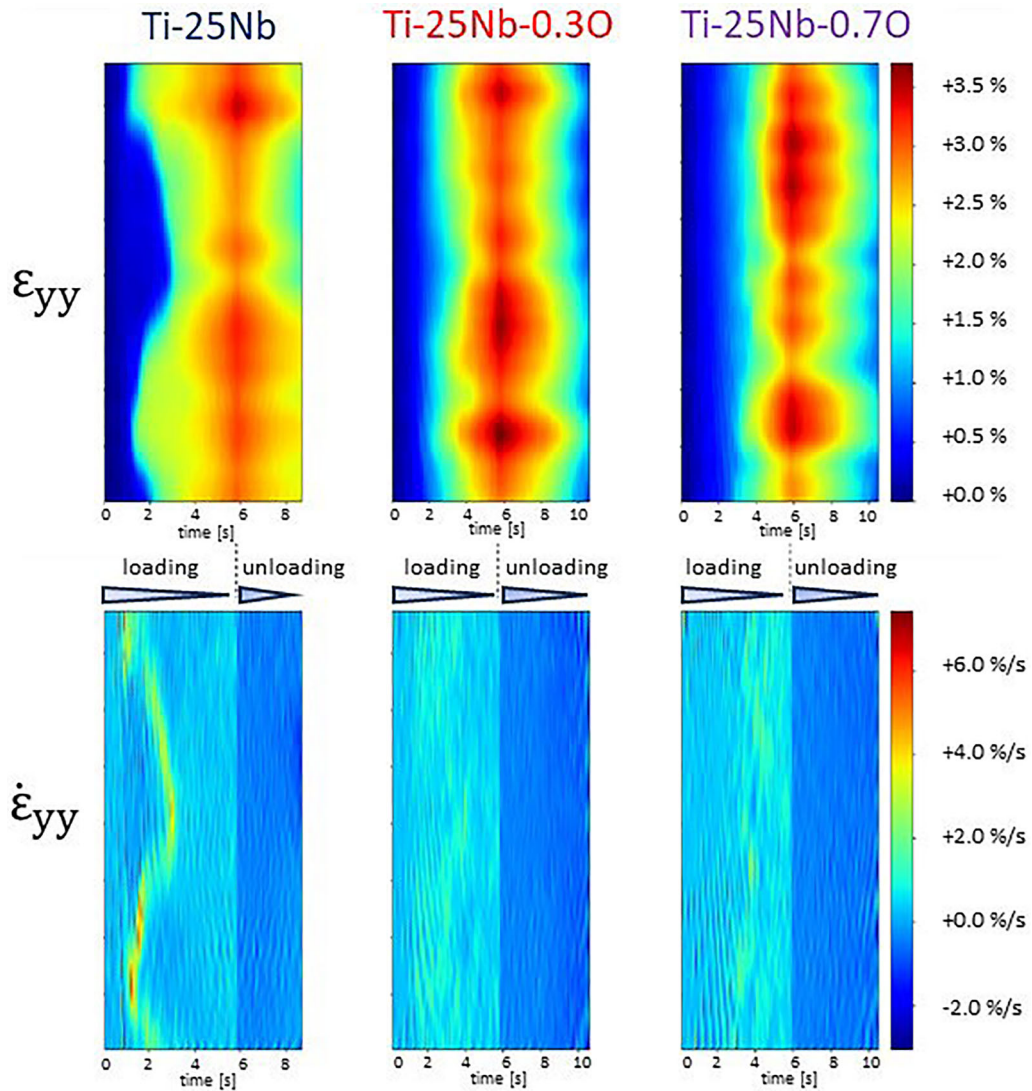


Fig. 10—Spatiotemporal graphs of Hencky strain ε_{yy} , and strain rate $\dot{\varepsilon}_{yy}$ of Ti-25Nb, Ti-25Nb-0.3O and Ti-25Nb-0.7O SMAs under load-unload tension.

transformation which propagated from the upper and lower parts of the gauge section towards the center of the specimen. During unloading, the Ti-25Nb SMA did not demonstrate localized reversible phase transformation which is in line with other studies confirming its shape memory property.

- (2) The superelastic Ti-25Nb-0.3O and Ti-25Nb-0.7O SMAs showed more discrete types of local deformation related to the activity of interstitial oxygen atoms, which hinders the stress-induced martensitic transformation.
- (3) Maximal local values of strain rate of the Ti-25Nb SMA were significantly (even over seven times) higher than those of global strain rate at particular stages of deformation. In the case of the Ti-25Nb-0.3O and Ti-25Nb-0.7O SMAs, maximal local values of strain rate were around

two times higher than those of global strain rate at particular stages of deformation.

ACKNOWLEDGMENTS

Karol M. Golasiński acknowledges the support of the Japan Society for the Promotion of Science (JSPS) Postdoctoral Fellowship (ID No. P20812) and the National Science Centre, Poland through the Grant 2023/48/C/ST8/00038. The authors would like to express their gratitude to Leszek Urbański from IPPT PAN for conducting tension tests.

CONFLICT OF INTEREST

The authors declare that they have no known competing financial interests or personal relationships that

could have appeared to influence the work reported in this paper.

OPEN ACCESS

This article is licensed under a Creative Commons Attribution 4.0 International License, which permits use, sharing, adaptation, distribution and reproduction in any medium or format, as long as you give appropriate credit to the original author(s) and the source, provide a link to the Creative Commons licence, and indicate if changes were made. The images or other third party material in this article are included in the article's Creative Commons licence, unless indicated otherwise in a credit line to the material. If material is not included in the article's Creative Commons licence and your intended use is not permitted by statutory regulation or exceeds the permitted use, you will need to obtain permission directly from the copyright holder. To view a copy of this licence, visit <http://creativecommons.org/licenses/by/4.0/>.

REFERENCES

1. M. Niinomi: *Mater. Sci. Eng. A*, 1998, vol. 243(1–2), pp. 231–36. [https://doi.org/10.1016/S0921-5093\(97\)00806-X](https://doi.org/10.1016/S0921-5093(97)00806-X).
2. M. Niinomi: *Metall. Trans. A*, 2002, vol. 33, pp. 477–86. <https://doi.org/10.1007/s11661-002-0109-2>.
3. M. Niinomi: *J. Mech. Behav. Biomed. Mater.*, 2008, vol. 1(1), pp. 30–42. <https://doi.org/10.1016/j.jmbbm.2007.07.001>.
4. M. Niinomi, M. Nakai, and J. Hieda: *Acta Biomater.*, 2012, vol. 8(11), pp. 3888–3903. <https://doi.org/10.1016/j.actbio.2012.06.037>.
5. S. Miyazaki, H.Y. Kim, and H. Hosoda: *Mater. Sci. Eng. A*, 2006, vol. 438–440, pp. 18–24. <https://doi.org/10.1016/j.msea.2006.02.054>.
6. H.Y. Kim and S. Miyazaki: *Shap. Mem. Superelast.*, 2016, vol. 2, pp. 380–90. <https://doi.org/10.1007/s40830-016-0087-7>.
7. K. Yamauchi, I. Ohkata, K. Tsuchiya and S. Miyazaki (Eds): *Shape Memory and Superelastic Alloys Applications and Technologies*. Woodhead Publishing Limited, Sawston, Cambridge, UK, 2011, pp. 15–41.
8. H.Y. Kim, Y. Ikehara, J.I. Kim, H. Hosoda, and S. Miyazaki: *Acta Mater.*, 2006, vol. 54, pp. 2419–29. <https://doi.org/10.1016/j.actamat.2006.01.019>.
9. M. Tahara, H.Y. Kim, T. Inamura, H. Hosoda, and S. Miyazaki: *Acta Mater.*, 2011, vol. 59, pp. 6208–18. <https://doi.org/10.1016/j.actamat.2011.06.015>.
10. M. Tahara, T. Inamura, H.Y. Kim, S. Miyazaki, and H. Hosoda: *Scripta Mater.*, 2016, vol. 112, pp. 15–18. <https://doi.org/10.1016/j.scriptamat.2015.08.033>.
11. J.A. Shaw and S. Kyriakides: *J. Mech. Phys. Solids*, 1995, vol. 43(8), pp. 1243–81. Doi: [https://doi.org/10.1016/0022-5096\(95\)00024-D](https://doi.org/10.1016/0022-5096(95)00024-D).
12. J.A. Shaw and S. Kyriakides: *Acta Mater.*, 1997, vol. 45(2), pp. 683–700. [https://doi.org/10.1016/S1359-6454\(96\)00189-9](https://doi.org/10.1016/S1359-6454(96)00189-9).
13. J.A. Shaw and S. Kyriakides: *Int. J. Plast.*, 1997, vol. 13(10), pp. 837–71. [https://doi.org/10.1016/S0749-6419\(97\)00062-4](https://doi.org/10.1016/S0749-6419(97)00062-4).
14. E.A. Pieczyska, S.P. Gadaj, W.K. Nowacki, and H. Tobushi: *Bull. Pol. Acad. Sci.*, 2004, vol. 52(3), pp. 165–71.
15. E.A. Pieczyska, S.P. Gadaj, W.K. Nowacki, and H. Tobushi: *Exp. Mech.*, 2006, vol. 46, pp. 531–42. <https://doi.org/10.1007/s11340-006-8351-y>.
16. E.A. Pieczyska, H. Tobushi, and K. Kulasiński: *Smart Mater. Struct.*, 2013, vol. 22(3), p. 035007. <https://doi.org/10.1088/0964-1726/22/3/035007>.
17. S. Daly, G. Ravichandran, and K. Bhattacharya: *Acta Mater.*, 2007, vol. 55(10), pp. 3593–4300. <https://doi.org/10.1016/j.actamat.2007.02.011>.
18. S. Miyazaki, T. Imai, K. Otsuka, and Y. Suzuki: *Scripta Mater.*, 1981, vol. 15(8), pp. 853–56. [https://doi.org/10.1016/0036-9748\(81\)90265-9](https://doi.org/10.1016/0036-9748(81)90265-9).
19. S. Miyazaki, K. Otsuka, and Y. Suzuki: *Scripta Mater.*, 1981, vol. 15(3), pp. 287–92. [https://doi.org/10.1016/0036-9748\(81\)90346-X](https://doi.org/10.1016/0036-9748(81)90346-X).
20. D. Delpueyo, A. Jury, X. Balandraud, and M. Grédiac: *Shap. Mem. Superelast.*, 2021, vol. 7, pp. 462–90. <https://doi.org/10.1007/s40830-021-00355-w>.
21. C. Bewerse, K.R. Gall, G.J. McFarland, P. Zhu, and L.C. Brinson: *Mater. Sci. Eng. A*, 2013, vol. 568, pp. 134–42. <https://doi.org/10.1016/j.msea.2013.01.030>.
22. C. Elibol and M.F.-X. Wagner: *Mater. Sci. Eng. A*, 2015, vol. 621, pp. 76–81. <https://doi.org/10.1016/j.msea.2014.10.054>.
23. C. Elibol and M.F.-X. Wagner: *Mater. Sci. Eng. A*, 2015, vol. 643, pp. 194–202. <https://doi.org/10.1016/j.msea.2015.07.039>.
24. B. Reedlunn, C.B. Churchill, E.E. Nelson, J.A. Shaw, and S.H. Daly: *J. Mech. Phys. Solids*, 2014, vol. 63, pp. 506–37. <https://doi.org/10.1016/j.jmps.2012.12.012>.
25. K.M. Golasinski, E.A. Pieczyska, M. Staszczak, M. Maj, T. Furuta, and S. Kuramoto: *Quant. InfraRed Thermogr. J.*, 2017, vol. 14(2), pp. 226–33. <https://doi.org/10.1080/17686733.2017.1284295>.
26. E.A. Pieczyska, M. Maj, K.M. Golasinski, M. Staszczak, T. Furuta, and S. Kuramoto: *Materials*, 2018, vol. 11(567), pp. 1–13. <https://doi.org/10.3390/ma11040567>.
27. K.M. Golasinski, M. Staszczak, and E.A. Pieczyska: *Materials*, 2023, vol. 16(9), p. 3288. <https://doi.org/10.3390/ma16093288>.
28. T. Saito, T. Furuta, J.H. Hwang, S. Kuramoto, K. Nishino, N. Suzuki, R. Chen, A. Yamada, K. Ito, Y. Seno, T. Nonaka, H. Ikehata, N. Nagasako, C. Iwamoto, Y. Ikuhara, and T. Sakuma: *Science*, 2003, vol. 300(5618), pp. 464–67. <https://doi.org/10.1126/science.1081957>.
29. S. Kuramoto, T. Furuta, J. Hwang, K. Nishino, and T. Saito: *Mater. Sci. Eng. A*, 2006, vol. 442(1–2), pp. 454–57. <https://doi.org/10.1016/j.msea.2005.12.089>.
30. S. Kuramoto, T. Furuta, J. Hwang, K. Nishino, and T. Saito: *Metall. Mater. Trans. A*, 2006, vol. 37A, pp. 657–62. <https://doi.org/10.1007/s11661-006-0037-7>.
31. S. Kuramoto, T. Furuta, J.W. Morris, N. Nagasako, E. Withey, and D.C. Chrzan: *Scr. Mater.*, 2013, vol. 68(10), pp. 767–72. <https://doi.org/10.1016/j.scriptamat.2013.01.027>.
32. L.S. Wei, H.Y. Kim, and S. Miyazaki: *Acta Mater.*, 2015, vol. 100, pp. 313–22. <https://doi.org/10.1016/j.actamat.2015.08.054>.
33. L.S. Wei, H.Y. Kim, T. Koyano, and S. Miyazaki: *Scr. Mater.*, 2016, vol. 123, pp. 55–58. <https://doi.org/10.1016/j.scriptamat.2016.05.043>.
34. K.M. Golasinski, E.A. Pieczyska, M. Maj, M. Staszczak, P. Świec, T. Furuta, and S. Kuramoto: *Arch. Civ. Mech. Eng.*, 2020, vol. 20(53), pp. 1–14. <https://doi.org/10.1007/s43452-020-00055-9>.
35. K.M. Golasinski, M. Maj, L. Urbański, M. Staszczak, A. Gradyś, and E.A. Pieczyska: *Quant. InfraRed Thermogr. J.*, 2023, <https://doi.org/10.1080/17686733.2023.2205762>.
36. K.M. Golasinski, E.A. Pieczyska, M. Maj, S. Mackiewicz, M. Staszczak, Z.L. Kowalewski, L. Urbański, M. Zubko, and N. Takesue: *Mater. Sci. Technol.*, 2020, vol. 36(9), pp. 996–1002. <https://doi.org/10.1080/02670836.2019.1629539>.
37. M. Nowak and M. Maj: *Arch. Civ. Mech. Eng.*, 2018, vol. 18, pp. 630–44. <https://doi.org/10.1016/j.acme.2017.10.005>.
38. S. Musiał, M. Nowak, and M. Maj: *Arch. Civ. Mech. Eng.*, 2019, vol. 19(4), pp. 1183–93. <https://doi.org/10.1016/j.acme.2019.06.007>.
39. M. Nowak, M. Maj, S. Musiał, and T. Płociński: *Mater. Sci. Eng. A*, 2020, vol. 790, p. 139725. <https://doi.org/10.1016/j.msea.2020.139725>.
40. S. Musiał, M. Maj, L. Urbański, and M. Nowak: *Int. J. Solids Struct.*, 2022, vol. 238, p. 111411. <https://doi.org/10.1016/j.ijsolstr.2021.111411>.

Publisher's Note Springer Nature remains neutral with regard to jurisdictional claims in published maps and institutional affiliations.